Application of a novel finite element method to design of splices in a fiber metal subjected to coupled thermo-mechanical loading

XueCheng Ping[1,*], **MengCheng Chen**[2], **BingBing Zheng**[1], **YiHua Xiao**[1]

[1] School of Mechanical and Electronical Engineering, East China JiaoTong University, 330013, China
[2] School of Civil Engineering, East China JiaoTong University, 330013, China
* Corresponding author: xuecheng_ping@yahoo.com.cn

Abstract The splice concept has been developed in fiber metal laminates (FMLs) due to the limited dimensions of pretreatment facility, the autoclave curing facility and C-scan facility. Failure always initiates in the splice opening between the metal splice edges before delamination occurs in the loading direction. In this paper, a novel finite element method for obtaining stress intensities is introduced in the estimation of the failure strength of splices in FMLs. A super wedge tip element for application to bi-material wedge is developed utilizing the numerical stress and displacement field solutions based on an ad hoc finite element eigenanalysis method, from which singular stress fields near apex of arbitrary bi-material wedges under coupled thermo-mechanical loading can be obtained. Failure of double spliced FMLs with varying spliced width and fiber-layer thickness were investigated, and fracture criterion based on stress intensity factors are presented to predict splice failure.

Keywords Thermo-mechanical loading, Fracture criterion, fiber metal laminate, Splice, Super wedge tip element

---

1. Introduction

Fiber metal laminates, such as Arall (Aramid reinforced aluminum laminates) and Glare (S2-glass fiber reinforced aluminum laminates), were developed at Delft University of Technology as a family of structural aerospace sheet materials. They take the advantages of metal alloys and fiber-reinforced composites providing superior mechanical properties [1], and have been applied to fuselage and leading edges in aircraft structures as a replacement of high-strength aluminum alloys due to their light weight, high strength, and excellent fatigue resistance. The dimensions of a FML are only limited by the width of the aluminum layers and not by their length. The available prepreg dimensions are also not limited. The maximum dimensions of a Glare skin panel are further limited by the dimensions of the pretreatment facility, the autoclave curing facility and C-scan facility. Also the handling and transportation of the panel may be a limiting factor. Currently only aluminium sheet with widths up to 1524 mm (60 inch) can be manufactured to the required accuracy with the necessary nominal thicknesses between 0.3 and 0.5 mm. This limitation would imply the necessity of applying many costly mechanical longitudinal or circumferential joints (at a maximum distance of 1524 mm) in an aircraft fuselage. To avoid this disadvantage, the internal splicing concept has been developed to increase the maximum available sheet size [2-4].

Due to the difference in elastic properties and thermal expansion coefficients of the components joined and discontinuity of junction geometry, residual stresses exist in each layer of the FML, and most importantly, high stress concentrations occur at the aluminum splice edges under thermal environment during manufacturing and coupled thermo-mechanical loading. As a result, the structural efficiency of bonded structures depends not on the structure itself but on splice strength. Generally, the failure behavior of the spliced FML always includes two steps, i.e., the onset of failure in the splice opening between the aluminum splice edges filled with resin during production of the material and the delamination extension in the loading direction.

Several researchers have developed theoretical concepts to describe the observed crack growth behaviour in fiber metal laminates [5-10]. These concepts start from the available methods for crack growth in monolithic aluminium sheets with additional parameters describing the bridging effect. In general, fatigue crack growth in a fiber metal laminate such as Glare is accompanied by delamination growth at the interface between the aluminium and glass fiber/adhesive layers. To incorporate this delamination growth in crack growth prediction methods, the energy release rate approach is applied to describe the delamination growth rate [7-10]. Few researchers have investigated the delamination behavior for different splicing geometries and layer thicknesses. Vries et al. [11] applied Griffith's energy criterion to calculate a delamination resistance, and Hashagen et al. [12] described the delamination in the interface by a plasticity based material model derived from a Hoffman-like yield function which bounds all states of stress in the interface. However, it is noticed that Vries et al. [11] and Hashagen et al. [12] only paid attention to the second falure processes, i.e., delamination between the prepeg layer and the aluminum layer, and the failure criterion for the splice opening between the aluminum splice edges has not been established. On the other hand, only the mechanical loading is considered in above researches, so that the established theories are not suitable for the bonded structures subjected to coupled thermo-mechanical loading.

In this paper, attempt is made to predict splice failures in fiber metal laminate subjected to coupled thermo-mechanical loading using stress singularity theory. In order to solve stress fields near the apex of bonded dissimilar materials as shown in Fig. 1, a super wedge tip element with numerical asymptotic solutions developed by Sze et al. [13] is firstly established and used for thermo-mechanical finite element analysis. Critical stress intensity factors are used as control parameters for fracture initiating at the bimaterial interface edge, and to predict fracture load for varying splice width and fiber layer thickness. The theoretical results are compared with experimental results for verification purposes.

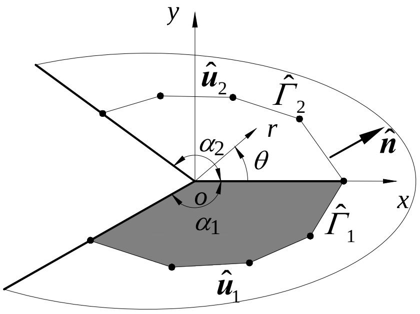

Fig. 1 Description of a bi-material wedge containing a super wedge tip element

2. Element stiffness matrix of the super wedge tip element

As shown in Fig. 1, a domain composed of bi-material sectors can be partitioned into inner and outer regions. The accurate solution to the entire domain requires coupling of the numerical solution in the inner region with that of the approximate solution through the finite element in the outer region. The coupling can be achieved by developing a super wedge tip element (as shown in Fig. 1) whose interpolation functions satisfy the governing equations exactly near the apex enforcing the inter-element displacement continuity along the common boundary and the nodes between the super and conventional elements. The stiffness matrix for the super wedge tip element of bi-material wedge under mechanical and thermal loading is obtained by considering the total potential expressed in the following form[15]

$$\begin{aligned}\Pi = &\sum_{k=1}^{2}\left\{-\frac{1}{2}\int_{\hat{\Gamma}_k} {}^{m}_{\lambda}\boldsymbol{\sigma}^{(k)T}\boldsymbol{n}^{T}\,{}^{m}_{\lambda}\boldsymbol{u}^{(k)}d\Gamma-\int_{\hat{\Gamma}_k} {}^{m}_{\lambda}\boldsymbol{\sigma}^{(k)T}\boldsymbol{n}^{T}\,{}^{\;\;\;\;t}_{\lambda+c}\boldsymbol{u}^{(k)}d\Gamma\right\}\\ &+\sum_{k=1}^{2}\left\{\int_{\hat{\Gamma}_k} {}^{m}_{\lambda}\boldsymbol{\sigma}^{(k)T}\boldsymbol{n}^{T}\hat{\boldsymbol{u}}^{(k)}d\Gamma-\int_{\hat{\Gamma}_k} {}^{*}\boldsymbol{t}^{(k)T}\hat{\boldsymbol{u}}^{(k)}d\Gamma\right\}+\Pi_0\end{aligned} \tag{1}$$

The terms ${}^{m}_{\lambda}\boldsymbol{\sigma}^{(k)}_{p}$, ${}^{m}_{\lambda}\boldsymbol{u}^{(k)}_{p}$ and ${}^{t}_{\lambda}\boldsymbol{\sigma}^{(k)}_{p}$, ${}^{t}_{\lambda}\boldsymbol{u}^{(k)}_{p}$ associated with the homogeneous solutions of mechanical and thermal loadings, respectively, and in the case of thermal loading, ${}^{t}_{c}\boldsymbol{\sigma}^{(k)}_{p}$ and ${}^{t}_{c}\boldsymbol{u}^{(k)}_{p}$ represent the known complementary solutions for non-singular stress and displacement fields. These vectors can be defined as

$${}^{m}_{\lambda}\boldsymbol{\sigma}^{(k)}_{p}=\boldsymbol{\Sigma}^{(k)}\,{}^{m}\boldsymbol{K},\quad {}^{m}_{\lambda}\boldsymbol{u}^{(k)}_{p}=\boldsymbol{U}^{(k)}\,{}^{m}\boldsymbol{K} \tag{2, 3}$$

$${}^{t}_{\lambda}\boldsymbol{\sigma}^{(k)}_{p}=\boldsymbol{\Sigma}^{(k)}\,{}^{t}\boldsymbol{K},\quad {}^{t}_{\lambda}\boldsymbol{u}^{(k)}_{p}=\boldsymbol{U}^{(k)}\,{}^{t}\boldsymbol{K} \tag{4, 5}$$

$${}^{t}_{c}\boldsymbol{\sigma}^{(k)}_{p}=\boldsymbol{F}^{(k)}_{c}(r,\theta)\boldsymbol{q}^{(k)}_{c},\quad {}^{t}_{c}\boldsymbol{u}^{(k)}_{p}=\boldsymbol{G}^{(k)}_{c}(r,\theta)\boldsymbol{q}^{(k)}_{c}+r\alpha_k\Delta T\boldsymbol{e}_r \tag{6, 7}$$

The details of $\boldsymbol{\Sigma}^{(k)}$ and $\boldsymbol{U}^{(k)}$ refer to Chen and Sze [14], and the definition of $\boldsymbol{F}^{(k)}_{c}$, $\boldsymbol{G}^{(k)}_{c}$, $\boldsymbol{q}^{(k)}_{c}$, $\boldsymbol{e}^{T}_{r}$ and ${}^{t}\boldsymbol{K}$ are listed in Barut et al. [15]. ΔT denotes the uniform temperature change. The unknown components of displacement vector along the common boundary segments, $\hat{\Gamma}_k$ (shown in Fig. 1), are denoted by $\hat{\boldsymbol{u}}^{(k)}$. ${}^{*}\boldsymbol{t}^{(k)}$ is the known applied traction components along the common boundary segments. $\boldsymbol{n}$ contains the components of the unite normal along $\hat{\Gamma}_k$. Π_0 represents the total potential associated with the known initial strain and stress components arising from thermal loading only. The vector of displacement components, $\hat{\boldsymbol{u}}^{(k)}$, along the common boundary between the global element and the conventional elements can be expressed in terms of the nodal displacement of the conventional elements as

$$\hat{\boldsymbol{u}}^{(k)}=\boldsymbol{L}\boldsymbol{v} \tag{8}$$

in which the matrix $\boldsymbol{L}$ contains the linear interpolation function compatible with those of the conventional elements. The vector $\boldsymbol{v}$ contains the nodal degrees of freedom associated with the conventional elements located on the boundary segment $\hat{\Gamma}_k$ of the super notch tip element.

Substituting for ${}^{m}_{\lambda}\boldsymbol{\sigma}^{(k)}_{p}$, ${}^{m}_{\lambda}\boldsymbol{u}^{(k)}_{p}$ and $\hat{\boldsymbol{u}}^{(k)}$ from Eqs. (2)-(8) into the expression for the total potential leads to

$$\Pi=-\frac{1}{2}\,{}^{m}\boldsymbol{K}^{T}\boldsymbol{H}\,{}^{m}\boldsymbol{K}-{}^{m}\boldsymbol{K}^{T}\,{}^{t}\boldsymbol{f}+{}^{m}\boldsymbol{K}^{T}\boldsymbol{G}\hat{\boldsymbol{v}}-\boldsymbol{v}^{T}\,{}^{*}\boldsymbol{f}+\Pi_0 \tag{9}$$

in which

$$\boldsymbol{H}=\sum_{k=1}^{2}\frac{1}{2}\int_{\hat{\Gamma}_k}\left[\boldsymbol{\Sigma}^{(k)T}\boldsymbol{Z}^{(k)T}_{\sigma}\boldsymbol{n}^{\mathrm{T}}\boldsymbol{Z}^{(k)}_{u}\boldsymbol{U}^{(k)}+\boldsymbol{U}^{(k)\mathrm{T}}\boldsymbol{Z}^{(k)T}_{u}\boldsymbol{n}\boldsymbol{Z}^{(k)}_{\sigma}\boldsymbol{\Sigma}^{(k)}\right]\mathrm{d}S,\quad \boldsymbol{G}=\sum_{k=1}^{2}\int_{\Gamma_{\mathrm{w}}}\boldsymbol{\Sigma}^{(k)T}\boldsymbol{Z}^{(k)T}_{\sigma}\boldsymbol{n}\boldsymbol{L}\,\mathrm{d}S$$

$${}^{t}\boldsymbol{f}^{(k)}=\sum_{k=1}^{2}\int_{\hat{\Gamma}_k}\boldsymbol{\Sigma}^{(k)T}\boldsymbol{Z}^{(k)T}_{\sigma}\boldsymbol{n}^{\mathrm{T}}\boldsymbol{Z}^{(k)}_{u}\,{}^{\;\;\;\;t}_{\lambda+c}\boldsymbol{u}^{(k)}_{p}d\Gamma,\quad {}^{*}\boldsymbol{f}^{(k)}=\sum_{k=1}^{2}\int_{\hat{\Gamma}_k}\boldsymbol{L}^{(k)}\,{}^{*}\boldsymbol{t}^{(k)}d\Gamma,\quad {}^{\;\;\;\;t}_{\lambda+c}\boldsymbol{u}^{(k)}_{p}={}^{t}_{\lambda}\boldsymbol{u}^{(k)}_{p}+{}^{t}_{c}\boldsymbol{u}^{(k)}_{p}$$

$\boldsymbol{Z}^{(k)}_{\sigma}$ and $\boldsymbol{Z}^{(k)}_{u}$ are the coordinate systerm transformation matrices. In order to express the total potential in terms of one unknown vector, $\boldsymbol{v}$, the first variation of the total potential with respect to

${}^{m}\boldsymbol{K}$ is taken. While noting that $\delta\Pi_0 = 0$, enforcing the first variation with respect to ${}^{m}\boldsymbol{K}$ to vanish results in

$$ {}^{m}\boldsymbol{K} = H^{-1}\left\{\boldsymbol{R}\boldsymbol{v} - {}^{t}\boldsymbol{f}\right\} \tag{10} $$

Substituting for ${}^{m}\boldsymbol{K}$ in the expression for the total potential, and enforcing the first variation of the total potential to vanish results in the nodal equations of equilibrium for the global element as

$$ \delta\Pi = \boldsymbol{v}^{T}\left\{\boldsymbol{K}_s\boldsymbol{v} - {}^{t}\boldsymbol{F} - {}^{*}\boldsymbol{f}\right\} = 0 \tag{11} $$

leading to

$$ \boldsymbol{K}_s\boldsymbol{v} = {}^{t}\boldsymbol{F} + {}^{*}\boldsymbol{f} \tag{12} $$

in which $\boldsymbol{K}_s$ and ${}^{t}\boldsymbol{F}$ are defined as $\boldsymbol{K}_s = \boldsymbol{G}^{T}\boldsymbol{H}^{-1}\boldsymbol{G}$ and ${}^{t}\boldsymbol{F} = \boldsymbol{G}^{T}\boldsymbol{H}^{-1}\,{}^{t}\boldsymbol{f}$. The vector ${}^{*}\boldsymbol{f}$ represents the internal loading vector at a node common to both the global and conventional elements. If a node is free of conventional elements, the components of the load vector represent the external force components. The vector ${}^{t}\boldsymbol{F}$ represents the reaction force that suppresses the deformation, resulting from thermal loading only, at the common nodes of global and conventional elements.

3. Experiment results

Fig. 2 shows a fiber metal laminate specimen with splices in interrupted aluminum layer edges. The materials comprising the specimen are aluminum, woven glass fiber reinforced composite and epoxy resin. Their elastic properties and coefficients of thermal expansion are listed in Tables 1 and 2. The thicknesses of aluminum layer and epoxy resin are all 1mm, the thickness of woven glass fiber reinforced composite varies as H=1, 2, 3, the width of splices vary as w=0.5, 1, 2, 3, 4, 5, 6, and the width of all layers are 20mm. Co-cured fiber metal laminate specimens were fabricated under the manufacture's recommended cure cycle for the composite material, and Fig. 3 illustrates the fabrication process.

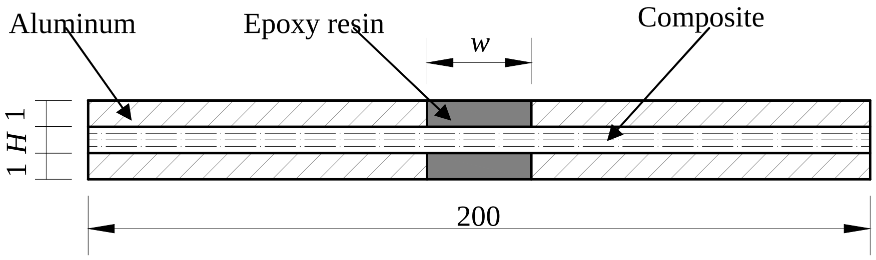

Figure 2. Dimensions of the spliced fiber metal laminate

Shimadzu EHF-EM electric-fluid serving tensile testing machine are used to test tension force, and Fig. 4 shows the tensile test apparatus. The load-displacement response curve obtained from the tensile test is linear until crack initiates at the splice, as shown in Fig. 5. Typical fractured fiber metal laminate specimens are shown in Fig. 6,by inspecting the fracture process, it is found that interface cracks initiate at the interface edge of the epoxy resin and the aluminum and propagate along the interface. Load bearing capacities F_{c} of the spliced fiber metal laminate specimens with varying splice width and fiber layer thickness are listed in Table 3. Experiment results show that, critical fracture load F_{c} increases with decreasing of splice width w, and decreases with increasing of fiber layer thickness *H*.

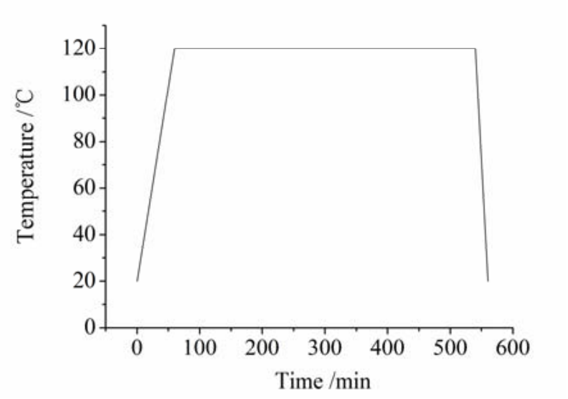

Figure 3. Cure cycle of the splices in a fiber metal laminate

Table 1. Material properties of the materials in the spliced fiber metal laminate

Materials	E_1	E_2	E_3	ν_{12}	ν_{13}	ν_{23}	G_{12}
Aluminum	72000	72000	72000	0.33	0.33	0.33	27067.67
Epoxy Resin	3200	3200	3200	0.49	0.49	0.49	1073.83
Composite	24600	24600	24600	0.025	0.363	0.025	1145

Table 2. Thermal expansion coefficients of the materials in the spliced fiber metal laminate

Materials	α_1(/°C)	α_2(/°C)	α_3(/°C)
Aluminum	1.881×10^{-5}	1.881×10^{-5}	1.881×10^{-5}
Epoxy Resin	5×10^{5}	5×10^{5}	5×10^{5}
Composite	6.443×10^{-6}	41.482×10^{-6}	6.443×10^{-6}

4. Fracture criterion of splices in a fiber metal laminate

Due to the symmetric feature of the structure, only one fourth of the structure is considered in the analysis. Fig. 7 illustrates the structure for FEM analysis and its boundary conditions. To solve the stress fields at the interface edge *o*, a 5-node super wedge tip element is used at this point, around which two-dimensional four-node element elements are used. Plane strain assumption is used in all numerical calculations.

Figure 4. Tensile test apparatus of the spliced fiber metal laminate

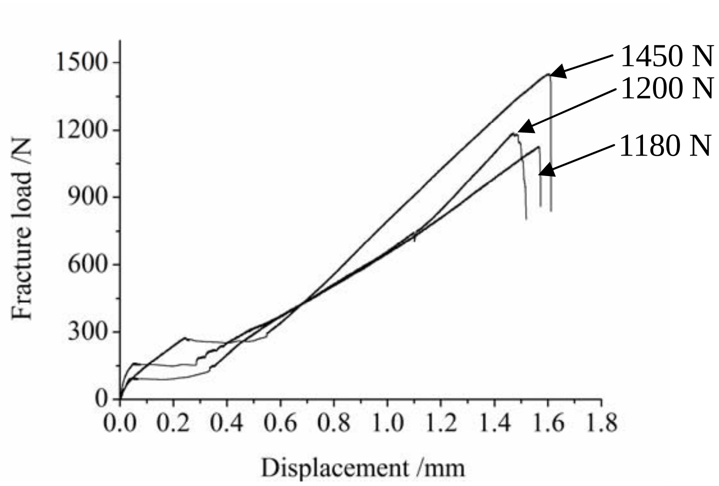

Figure 5. Load-displacement curves for *w*=4mm and *H*=1mm

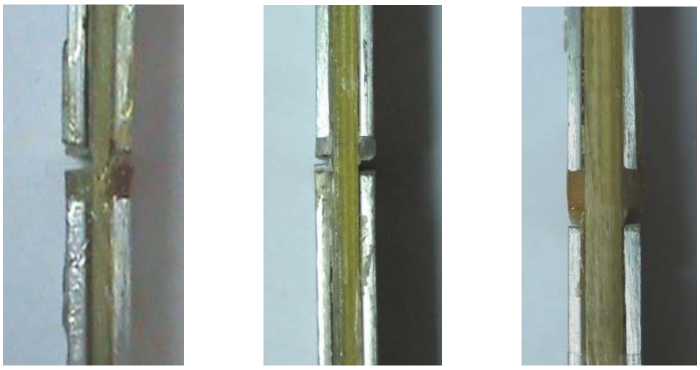
(a) (b) (c)

Figure 6. Specimens after fracture at the splices for: (a) *H*=1mm; (b) *H*=2mm; *H*=3mm;

Residual thermal stresses exist in specimens because a heat cure cycle is used, so during tensile test experiment, the specimens are actually subjected to thermo-mechanical coupled loading. If crack initiation load at the splices is determined by the stress intensity at the interface edge *o*, a suitable stress intensity parameter should be established, and the critical value of this parameter should be a constant. In other word, under coupled thermo-mechanical loading, crack will initiate when the stress intensity parameter at the interface edge reaches its critical value.

For the interface edge configuration at point *o* shown in Fig. 7, the method presented in Section 2 is applied to solve the intensity of stress fields. The singularity exponent can be obtained as λ=-0.34768 by using the finite element eigenanalysis method [13, 14]. Its corresponding angular variation of stress $\bar{\sigma}_{ij}(\theta)$ is plotted in Fig. 8. After the coefficient $\boldsymbol{q}_c^{(k)}$ is solved based on the continuity conditions across the interfaces and the traction-free conditions across the free edges, the regular stress terms near the interface edge can be obtained by Eq. (7). Fig. 9 illustrates the regular stress terms. Because there is only one singularity exponent, the stress field near interface edge *o* can be expressed as:

$$\sigma_{ij}(r,\theta) = K \cdot r^{\lambda} \cdot \bar{\sigma}_{ij}(\theta) + {}^{t}_{c}\sigma_{ij}(\theta) \qquad (13)$$

where $\sigma_{ij}^{FE}(r,\theta)$ is the stress field near interface edge calculated from the present FEM analysis. If the stress intensity factor K, a summation of ${}^{m}K$ and ${}^{t}K$, can be used as interface edge fracture cretirion, the local falure condition will be

$$K \geq K_{\mathrm{c}} \tag{14}$$

Table 3. The Fracture loading of specimens with various splice width and fiber layer thickness

Splice width w (mm)	Fracture load F_{c} (N)		
	H=1 mm	H=2 mm	H=3 mm
0.5	2096.67	2041.38	1684.29
1	1706.67	1169.30	451.20
2	1456.67	1025.40	357.40
3	1320.00	1016.62	685.08
4	1276.67	1005.02	859.29
5	1343.33	996.10	861.48
6	1306.67	1002.40	912.00

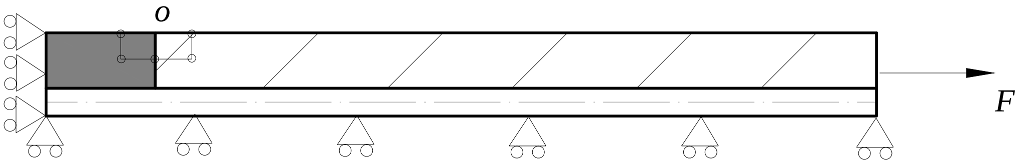

Figure 7. One quarter of a specimen and its boundary conditions

Fig. 10 shows the calculated critical stress intensity factor under coupled thermo-mechanical loading. The thermal loading is ΔT=-100°C, and the critical mechanical loadings corresponding to differenent splice width and fiber layer thickness are listed in Table 3. From Fig. 10, it can be seen that, K_{c} varies in a little range, which is about from 26.6 to 29.6MPa·mm$^{0.34768}$. The above results indicates that K_{c} nearly keeps unchanged regardless of the change of local structure, and can be used as the fracture control parameter.

The stress intensity factor at interface edges is closely related to the external thermo-mechanical loads. It is necessary to find the relationship between them. As seen from Table 3, critical load varies monotonously as the splice width and fiberlayer thickness change, and K_{c}, which is a constant value, can't be used directly to predict critical load. Obviously, the stress intensity factor ${}^{m}K_{\mathrm{c}}$ caused by mechanical loading should be proportional to the mechanical loading imposed. According to this principle, the critical tensile load F_{c} can be predicted as

$$F_{\mathrm{c}} = {}^{m}K_{\mathrm{c}} \times F_{\mathrm{c}}\big|_{w=6,H=1} / {}^{m}K_{\mathrm{c}}\big|_{w=6,H=1} \times S / S\big|_{H=1} \tag{15}$$

where ${}^{m}K_{\mathrm{c}} = K_{\mathrm{c}} - {}^{t}K$, K_{c} is critical stress intensity factor when w is taken as 6 mm and H is taken as 1 mm, ${}^{t}K$ is the critical stress intensity factor under thermal loading of ΔT=-100°C, S is the cross section area of specimens. Figs. 11 and 12 show the critical stress intensity factor and critical tensile load, respectively. The experimental values of stress intensity factors shown in Fig. 11 are obtained by using critical tensile loads tested from experiments. From Fig. 12, it can be seen that the predicted critical mechanical loads are in good agreement with experimental values. Based on the predicted values of stress intensity factors, the relationship between external loads and local stresses at interface edges of the splices is established. For various kinds of structures, Eq. (15) can predict the critical mechanical load, and it is not neccesary to experimentally determine them one by one.

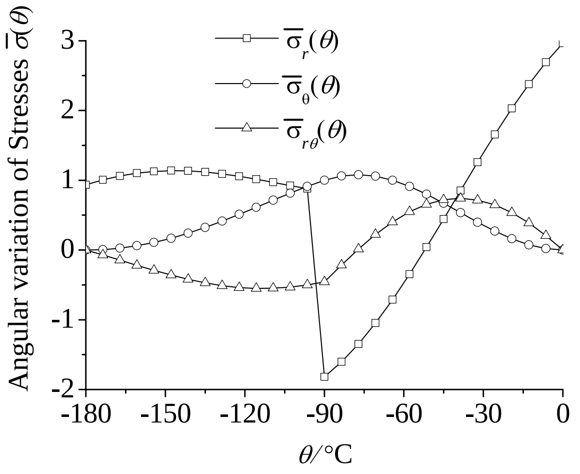

Figure 8. Angular variation of tresses around the interface edge *o*

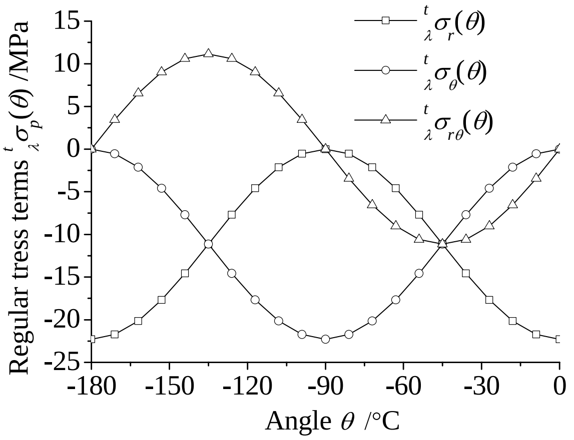

Figure 9. Regular stress terms around the interface edge *o*

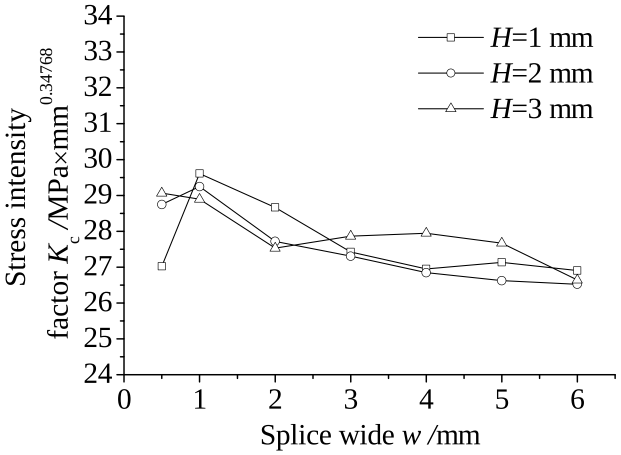

Figure 10. Critical stress intensity factor K_c of the interface edge *o*

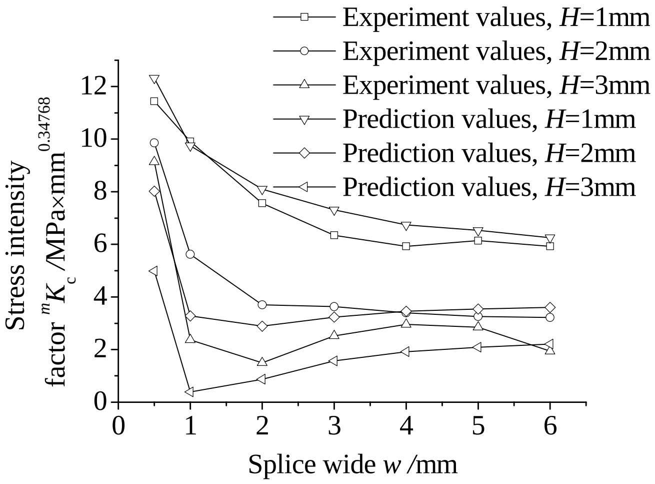

Figure 11. Critical stress intensity factor ${}^{m}K_{\mathrm{c}}$ of the interface edge *o*

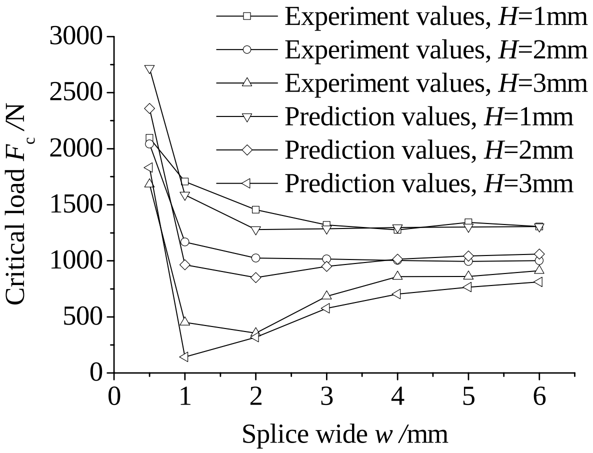

Figure 12. Critical load F_{c} of the interface edge *o*

5. Conclusions

The fracture behaviors of the splices in fiber metal laminates are investigated. The states of stresses at the interface edges of splices are analyzed based on a novel finite element method. A stress intensity factor based fracture criterion for the splice failure is established to predict critical tensile load. Through the results in this study, the following conclusions are drawn:

1) The critical stress intensity factor K_{c} under coupled thermo-mechanical loading can be used as local fracture criterion for the interface edges of the splices.
2) The critical stress intensity factor ${}^{m}K_{\mathrm{c}}$ under mechanical loading can be used to predict the critical mechanical loading F_{c}.
3) Because the decrease of the splice width *w* will lead to the reduction of the stress intensity factor ${}^{t}K$ induced by residual thermal stresses, so it will make ${}^{m}K_{\mathrm{c}}$ increase. Consequently, the critical mechanical loading F_{c} will increases.
4) Because the increase of the fiber-layer thickness *H* will lead to the increase of the stress intensity factor ${}^{t}K$ induced by residual thermal stresses, so it will cause ${}^{m}K_{\mathrm{c}}$ to reduce. Consequently, the critical mechanical loading will decrease.

Acknowledgements

This study was sponsored by the National Natural Science Foundation of China under Grant No.51065008 and No.10662004, the Natural Science Foundation of Jiangxi Province under Grant No.2010GZW0013 and the Jinggang-Star training Plan for Young Scientists of Jiangxi Province under Grant No. 20112BCB23013.

References

[1] A. Vlot, J.W. Gunnink, Fiber metal laminates-an introduction. USA: Kluwer Academic Publisher, 2001.

[2] C.A.J.R. Vermeeren, T.H. Beumler, J.L.C.G. De Kanter, O.C. Van Der Jagt, B.C.L. Out, Glare design aspects and philosophies. Appl Comp Mat, 10(2003) 257-276.

[3] T.J. de Vries, A. Vlot, F. Hashagen, Delamination behavior of spliced Fiber Metal Laminates. Part 1. Experimental reslts. Comp Struct, 46(1999)131-145.

[4] F. Hashagen, R. de Borst, T. de Vries, Delamination behavior of spliced Fiber Metal Laminates. Part 2. Numerical investigation. Comp Struct, 46(1999) 147-162.

[5] T. Takamatsu, T. Shimokawa, T. Matsumura, Y. Miyoshi, Y. Tanabe, Evaluation of fatigue crack growth behaviour of Glare3 fiber/metal laminates using compliance method. Eng Fract Mech, 70(2003)2603-2616.

[6] Y.J. Guo, X.R. Wu, A phenomenological model for predicting crack growth in fiber-reinforced metal laminates under constant amplitude loading. Comput Sci Technol, 59(1999)1825-1831.

[7] R.C. Alderliesten, J. Schijve, S. van der Zwaag, Application of the energy release rate approach for delamination growth in Glare. Eng Fract Mech, 73 (2006) 697-709.

[8] R.C. Alderliesten, Analytical prediction model for fatigue crack propagation and delamination growth in Glare. Int J Fatigue, 29(2007) 628-646.

[9] P.Y. Chang, J.M. Yang, Modeling of fatigue crack growth in notched fiber metal laminates. Int J Fatigue, 30(2008)2165-2174.

[10] Marcela V. Cid Alfaro, Akke S.J. Suiker, Rene de Borst, Joris J.C. Remmers, Analysis of fracture and delamination in laminates using 3D numerical modeling. Eng Fract Mech, 76(6)(2009) 761-780.

[11] T.J. de Vries, A. Vlot, F. Hashagen, Delamination behavior of spliced Fiber Metal Laminates. Part 1. Experimental results. Comp Struct 46 (1999) 131-145.

[12] F. Hashagen, R. de Borst, T. de Vries, Delamination behavior of spliced Fiber Metal Laminates. Part 2. Numerical investigation. Comp Struct 46 (1999) 147-162.

[13] K.Y. Sze, H.T. Wang, H. Fan, A finite element approach for computing edge singularities in piezoelectric materials. Int J Solids Struct, 38(2001) 9233-9252.

[14] M.C. Chen, K.Y. Sze, A novel hybrid finite element analysis of bimaterial wedge problems. Eng Fract Mech, 68(2001)1463-1476.

[15] A. Barut, I. Guven, E. Madenci. Analysis of singular stress fields at junctions of multiple dissimilar materials under mechanical and thermal loading. Int J Solids Struct, 38(2001) 9077-9109.